

Quantitative Comparison of Fine-Tuning Techniques for Pretrained Latent Diffusion Models in the Generation of Unseen SAR Image Concepts

Solène Debuysère^a, Nicolas Trouvé^a, Nathan Letheule^a, Olivier Lévêque^a, Elise Colin^a

^aONERA - The French Aerospace Lab, Paris-Saclay University, Palaiseau, France

Abstract

This work investigates the adaptation of large pre-trained latent diffusion models to a radically new imaging domain: Synthetic Aperture Radar (SAR). While these generative models, originally trained on natural images, demonstrate impressive capabilities in text-to-image synthesis, they are not natively adapted to represent SAR data, which involves different physics, statistical distributions, and visual characteristics. Using a sizeable SAR dataset (on the order of 100,000 to 1 million images), we address the fundamental question of fine-tuning such models for this unseen modality. We explore and compare multiple fine-tuning strategies, including full model fine-tuning and parameter-efficient approaches like Low-Rank Adaptation (LoRA), focusing separately on the UNet diffusion backbone and the text encoder components. To evaluate generative quality, we combine several metrics: statistical distance from real SAR distributions, textural similarity via GLCM descriptors, and semantic alignment assessed with a CLIP model fine-tuned on SAR data. Our results show that a hybrid tuning strategy yields the best performance: full fine-tuning of the UNet is better at capturing low-level SAR-specific patterns, while LoRA-based partial tuning of the text encoder, combined with embedding learning of the <SAR> token, suffices to preserve prompt alignment. This work provides a methodical strategy for adapting foundation models to unconventional imaging modalities beyond natural image domains.

1. Introduction

Synthetic Aperture Radar (SAR) imaging is playing an increasingly central role in remote sensing, thanks to its unique physical properties and the rapidly expanding ecosystem of sensors. Unlike optical systems, SAR is an active sensor that transmits its own signal, enabling image acquisition regardless of lighting conditions. This independence from ambient illumination makes SAR particularly well-suited for continuous, all-weather monitoring. Additionally, SAR signals can penetrate certain materials such as vegetation, sand, or dry snow, giving access to information inaccessible to optical sensors. These characteristics, combined with a growing diversity of platforms, from small satellites to airborne or drone systems operating across different frequency bands, have established SAR as a key modality for various applications, including surveillance, environmental monitoring, urban mapping, and disaster assessment.

However, SAR images exhibit fundamental differences from natural optical images. First, the imaging geometry is non-conventional: SAR data is acquired in a slant-range and azimuth coordinate system, introducing distortions that depend on viewing angle and terrain relief. Second, SAR amplitude values are not governed by Gaussian distributions but instead follow speckle statistics, due to the interference phenomena intrinsic

to coherent systems. This results in highly textured images and heavy-tailed statistical distributions. Moreover, the radiometric content of SAR images spans a wide dynamic range, with bright reflections (e.g., from man-made structures or double-bounce effects) coexisting with very low-return regions (e.g., calm water). These properties are further modulated by acquisition parameters such as polarization, incidence angle, resolution, and wavelength, making SAR data complex to model.

This diversity and variability challenge conventional computer vision methods, particularly those developed and trained on optical imagery. One promising direction lies in the simulation of SAR data, which enables algorithm testing, rare scenario generation, and dataset augmentation. Recent advances in generative models, especially diffusion-based approaches, have revived interest in image synthesis. Diffusion models have been shown to surpass GANs in realism and diversity.

Among these, latent diffusion models represent a reference class of generative models. Instead of performing the denoising process directly in pixel space — which is computationally intensive and less efficient for high-resolution data — they work in a compressed space called the latent space. This latent space is learned through a Variational Autoencoder (VAE), whose encoder maps images into lower-dimensional representations, and whose decoder reconstructs images from this space. The generative process itself is handled by a UNet-based denoising network, trained to reverse a noise corruption process (called forward diffusion process) in the latent domain. This reverse diffusion process is conditioned on text embeddings produced by text encoders, which allows the model to associate semantic meaning with the denoising trajectory. These models, when

*Corresponding author.

Email addresses: solene.debuysere@onera.fr (Solène Debuysère), nicolas.trouve@onera.fr (Nicolas Trouvé), nathan.letheule@onera.fr (Nathan Letheule), olivier.leveque@onera.fr (Olivier Lévêque), elise.colin@onera.fr (Elise Colin)

pretrained on massive optical datasets, become powerful generative priors, capable of synthesizing photorealistic scenes and semantically coherent layouts. However, they lack any native knowledge of SAR-specific image structures, noise patterns, or physical signal distributions.

In this work, we explore the adaptation of such a pre-trained latent diffusion model to the SAR modality. Starting from a domain-specific dataset of approximately 100,000 high-resolution airborne SAR images, acquired with ONERA’s SETHI sensor, we aim to investigate how such a model can be fine-tuned to synthesize realistic radar imagery from textual prompts. The scale of this dataset places us in an intermediate regime: substantially larger than typical few-shot setups, yet considerably smaller than the hundreds of millions of samples used for pretraining foundation models, making it a relevant test case for transfer learning strategies.

This brings us to a central question: what fine-tuning strategy should be employed to effectively adapt a pre-trained model to such an unfamiliar modality? Should all components of the model be retrained, or can we rely on more lightweight approaches such as Low-Rank Adaptation (LoRA) to update only a subset of parameters? To answer this, we carry out a comparative study of several fine-tuning strategies, applied selectively to the text encoder and the UNet diffusion backbone.

An equally important challenge is how to evaluate the quality of generated SAR images. Traditional visual metrics are ill-suited to this task, as they assume natural image statistics. In response, we propose a new evaluation framework, combining statistical distribution comparisons, texture analysis via Gray-Level Co-occurrence Matrices, and semantic alignment using a CLIP model fine-tuned on SAR-caption pairs.

The remainder of the paper is organized as follows. We begin by reviewing related work in generative modeling and fine-tuning approaches, with a focus on parameter-efficient adaptation methods. We then describe the construction of our SAR dataset and the pre-processing pipeline applied to the SETHI archive. The methodological section details the diffusion model architecture, the fine-tuning strategies considered, and our proposed evaluation metrics. This is followed by a presentation of our experimental results, including both quantitative analyses and visual examples of generated SAR images. We conclude with a discussion of our findings, limitations, and perspectives for future work.

2. Related work

Recent years have seen the emergence of large-scale generative models capable of synthesizing images from natural language prompts. These models, commonly referred to as foundation models, are typically pre-trained on massive datasets and designed to capture high-level semantic alignment between visual and textual modalities. Their success has led to interest in adapting them to specialized domains, such as medical imaging or remote sensing. However, extending these models to unconventional modalities such as SAR, which differs both structurally and statistically from natural images, remains a largely underexplored challenge. In this section, we review the relevant efforts

in basic vision language modeling and the fine-tuning strategies developed to adapt them effectively.

2.1. Foundation Generative Vision-Language Models

Vision-Language Models (VLMs) have demonstrated strong capabilities in learning joint embeddings and generative alignments across visual and textual modalities. Early models such as CoCa [1] combine contrastive and generative objectives to jointly align and synthesize, while more recent architectures like CM3Leon and Chameleon [2] implement early fusion designs, allowing unified multimodal generation through transformer-based architectures. These systems can generate both image and text outputs conditioned on joint multimodal inputs.

In parallel, a distinct family of models specifically focuses on text-to-image generation. Within this space, Stable Diffusion [3], Flux [4], Imagen [5], and Parti [6] represent several lines of research exploring different generation mechanisms: respectively, latent-space diffusion, pixel-space diffusion, and autoregressive modeling. Among them, latent diffusion models such as Stable Diffusion have gained attention for their ability to generate high-resolution images with lower computational cost. This is achieved by operating in a compressed latent space, learned via a Variational Autoencoder (VAE), rather than directly in pixel space.

Stable Diffusion XL (SDXL) [7], in particular, is a flexible, open-source latent diffusion model consisting of three main components: (i) a VAE that compresses images into latent representations, (ii) a dual text encoder pipeline to transform prompts into embeddings, and (iii) a UNet backbone that performs conditional denoising in the latent domain. Numerous extensions have been proposed to control its generation process, including spatial guidance methods such as ControlNet [8], and global image-based conditioning methods like IP-Adapter [9]. However, current research has mostly focused on natural image domains, and little is known about the model’s ability to learn physically grounded or domain-specific concepts such as those present in SAR imagery.

2.2. Fine-tuning approaches

As the size of pre-trained Vision-Language Models (VLMs) continues to grow, full fine-tuning—i.e., updating all model parameters—becomes increasingly impractical due to memory, compute, and data constraints. To address this, a family of Parameter-Efficient Fine-Tuning (PEFT) techniques has emerged, aiming to adapt large-scale models by updating only a small fraction of their weights parameters.

One of the most widely used PEFT strategies is Low-Rank Adaptation (LoRA) [10], which injects trainable low-rank matrices into the linear layers of the model. LoRA enables effective adaptation while keeping the majority of weights frozen, drastically reducing memory usage. Extensions such as QLoRA [11] and DoRA [12] further optimize efficiency by combining low-rank decomposition with quantization or weight reparameterization, especially for large language models (LLMs), and are increasingly being explored in vision and multimodal settings.

Other approaches focus on prompt-level conditioning rather than internal parameter modification. Prompt-based tuning methods such as CoOp [13] and VPT [14] learn input embeddings or prompts that guide the model without altering its architecture. These techniques are lightweight and adaptable, but may can't represent entirely new visual domains when semantic gaps are large.

In contrast, DreamBooth [15] enables explicit concept injection by associating new visual identities or styles with custom textual tokens. This method has been successfully applied to generate highly specific outputs from small datasets — for instance, [16] fine-tuned Stable Diffusion 3 on 300 samples of Jamini Roy-style paintings, achieving culturally accurate synthesis. Further control can be obtained using ControlNet and IPAdapter, which allow generation to be conditioned on structural priors such as edge maps, segmentation, or depth — especially effective for layout-sensitive domains.

Another promising method is textual inversion [17], which learns new visual concepts directly in the embedding space of the text encoder, without modifying the image generator. When combined with DreamBooth and LoRA, as in [18], it enables joint control over modality and identity — for example, generating paired visible-infrared images from shared prompts like "a [modality] photo of a [person] person".

Collectively, these techniques have made it feasible to adapt powerful diffusion models such as Stable Diffusion to novel visual concepts, ranging from new objects to artistic styles, while requiring relatively modest amounts of data and compute. However, most existing applications remain confined to natural image domains, and focus on concept categories that are semantically close to those seen during pre-training (e.g., human faces, animals, or art styles). The adaptation of foundation models to structurally and statistically distinct modalities — such as depth images, medical scans, or Synthetic Aperture Radar (SAR)—remains a largely unexplored and technically challenging frontier.

2.3. Generative Foundation models in Remote Sensing

In the field of remote sensing, most recent generative Vision-Language Models (VLMs) have focused primarily on optical imagery, with limited or no support for Synthetic Aperture Radar (SAR) data. Several foundation models have been trained from scratch on large-scale optical satellite image datasets, including RS5M and GeoRSCLIP [19], DiffusionSat [20], MetaEarth [21], CRS-Diff [22], and HSiGene [23], the latter targeting hyperspectral image generation. While most of these models are trained for representation learning, zero-shot classification, or retrieval in the optical domain, only a few are designed for image generation — and even fewer extend to radar-based modalities such as Synthetic Aperture Radar (SAR).

To our knowledge, Text2Earth [24] is the first foundation model that incorporates both SAR and optical data for text-to-image generation. However, its SAR component relies on synthetic radar - like images produced via Pix2Pix translation from RGB inputs, rather than using real SAR measurements that include speckle noise, geometric distortions, and backscatter

- specific statistical properties. As such, the model does not capture the full complexity of radar signal characteristics.

Other models, such as SARChat-InternVL2.5-8B [25], have focused on improving multimodal understanding of SAR imagery through conversational tasks like description, counting, or spatial reasoning. However, this model is not able to do image generation, and its training data is limited to open-source object detection benchmarks. It does not address large-scale SAR image synthesis nor generalization across acquisition conditions.

In general, the development of generative foundation models for SAR remains in its infancy, especially for high-resolution data and for tasks beyond classification or detection. While some efforts have explored training from scratch, such approaches are computationally prohibitive and require extensive domain - specific data. In contrast, adapting pre-trained generative models - originally trained on optical images - to the SAR domain via fine-tuning offers a more scalable and practical alternative. Yet, this path remains largely underexplored. Our work positions itself in this gap, investigating how such pre-trained models can be effectively adapted to synthesize realistic SAR imagery guided by textual prompts.

3. Dataset Creation

Unlike optical imaging, SAR systems actively transmit radar pulses toward the ground and record the backscattered signals. While optical image resolution is defined by the number of pixels per unit area, SAR images have two distinct resolutions: one in the range direction (perpendicular to the flight path) and one in the azimuth direction (along the flight path). SAR image formation involves two key steps: *range compression*, which enhances resolution perpendicular to the sensor trajectory, and *azimuth compression*, which improves resolution along the sensor motion. These processes rely on advanced signal processing techniques, such as the use of frequency - modulated pulses (chirps) and coherent integration of successive returns to synthesize a larger effective antenna aperture.

In our dataset, the resulting images are stored in what is known as the Single Look Complex (SLC) format, which means that images are acquired in the antenna reference frame, known as “slant range-azimuth” coordinate system, which is link to the radar’s viewing geometry rather than geographic axes. As a result, SAR images are rotated with respect to true North. They are also geometrically distorted because the sampling in azimuth and slant-range directions does not correspond to equal ground distances. This leads to visual effects where structures like roads or rivers appear tilted or compressed when overlaid on optical images. For instance, in our example (see Figure (d) 1), the SAR image appears diagonally inserted within the optical scene due to the acquisition in slant-range geometry during an ascending right-looking orbit.

At ONERA’s DEMR department, we conduct airborne campaigns using the SETHI radar system and process raw radar echoes into SLC-format SAR images (each approximately 40,000 × 7000 complex pixels). From this large archive, we built a train-

ing dataset by applying several post-processing steps to raw complex and amplitude images.

Pre-processing Raw Data. To ensure data quality, we first filtered the dataset by selecting images with sufficient metadata, choosing only those acquired in the X-band (8 to 12 GHz) and with HH or VV polarization, while excluding small or geographically overlapping scenes. The calibration factors were then applied to ensure radiometric accuracy. Then, we apply a correction matrix to complex images to refocus the spectrum in both directions to correct spectral misalignment caused by acquisition conditions. Finally, all images were downsampled in the frequency domain to a target resolution of 40 cm (in both azimuth and range directions).

Training Dataset Creation. Our final dataset consists of refocused and resampled SAR images stored as complex-valued matrices. For training purposes, we work on amplitude images, whose pixel values follow a Rayleigh distribution — unbounded and highly skewed, with a small proportion (1–3%) of very high-intensity scatterers. These bright pixels are critical as they correspond to strong reflectors such as buildings or metallic structures. For visualization and learning stability, we apply the following normalization:

$$A(r, y)_{\text{norm}} = \frac{A(r, y)}{\mu + 3 \cdot \sigma} \quad (1)$$

where $A(r, y)$ is the amplitude value at coordinates (r, y) , and μ and σ are the mean and standard deviation of the amplitude image, respectively. Then, we clip values between 0 and 1, ensuring that 98% of the values fall within this interval. This results in all pixels beyond the threshold are "flattened" at exactly 1. This creates an artificial saturation at pixel value 1.

The normalized images are then cropped into standardized patches of size 1024×1024 pixels. For a subset of these patches, we created geo-aligned SAR–optical image pairs using optical imagery from the IGN database. Textual descriptions were automatically generated for the optical images using the foundation model CogVLM2 [26].

Because the statistical distribution of SAR amplitudes depends heavily on scene type, we categorized the dataset into semantic classes (e.g., forest, water, city) based on a manually constructed keyword dictionary applied to the generated captions. The class distribution is presented in Figure 2. We note that some mislabeling may occur due to inaccuracies in captioning or ambiguity in keyword matching. These class labels were aggregated for visualization and analysis.

Finally, we performed a cleaning stage to remove low-quality samples, such as blurred zones, blank images, and noisy or distorted data.

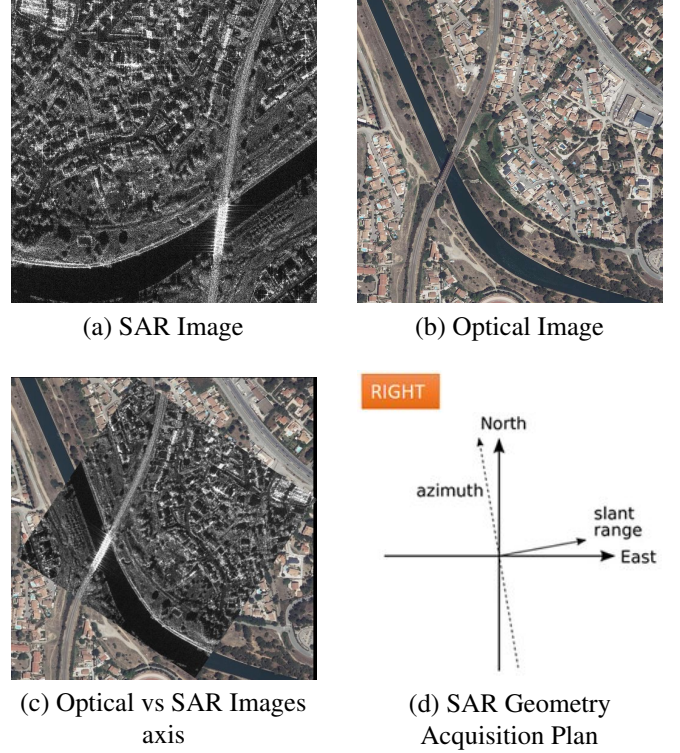


Figure 1: Pairs of optical (ground plan) and SAR (slant-range plan) images.

4. Methodology

4.1. Stable Diffusion framework

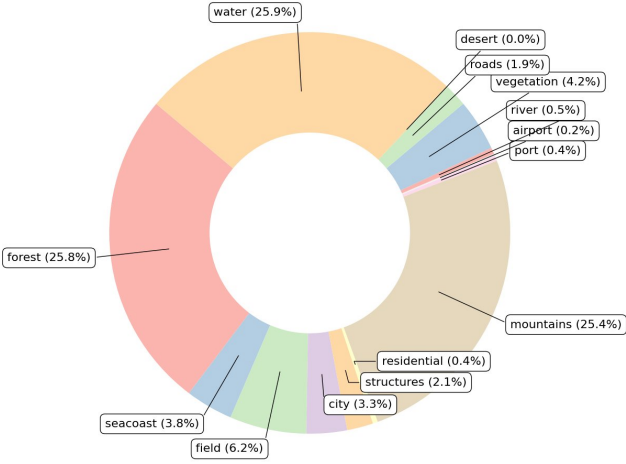
Input–Output Representation. The model operates in a latent space rather than directly in pixel space. Text–image pairs are processed independently into compact latent representations. First, a Variational Autoencoder (VAE) encodes an image x into a latent representation z :

$$z = E(x), \quad \tilde{x} = D(z) \quad (2)$$

where E and D denote the encoder and decoder, respectively. The image is typically compressed by a factor of 8 along each spatial dimension. In parallel, the text prompt y , which describes the scene to be generated, is embedded into a semantic vector space via the model’s text encoders, yielding embeddings $\tau_\theta(y)$.

Stable Diffusion XL (SDXL) employs two separate text encoders. *Text Encoder 1* (CLIP ViT-L) produces token-level embeddings of shape $[B, 77, 768]$ — one vector per token. These embeddings are used in the UNet’s cross-attention layers for fine-grained conditioning. *Text Encoder 2* (OpenCLIP ViT-bigG) also provides token-level embeddings, but in higher dimension $[B, 77, 1280]$, and additionally produces a global [CLS] token, which is passed through a learned linear projection to generate a global caption embedding, noted as `text_embeds`. This projection complements the token-level conditioning and is injected globally into the UNet at each layer.

The token - wise embeddings from both encoders are concatenated to form a $[B, 77, 2048]$ tensor, injected into each UNet



Category	Train	Validation	Test
Airport	0.17	0.16	0.23
City	3.27	3.13	3.33
Desert	0.01	0.01	0.01
Field	6.20	6.23	6.04
Forest	25.82	25.90	25.82
Mountains	25.36	25.44	25.46
Port	0.42	0.40	0.53
Residential	0.40	0.46	0.41
River	0.51	0.64	0.57
Roads	1.88	1.78	1.80
Seacoast	3.82	3.57	3.73
Structures	2.11	2.06	2.05
Vegetation	4.16	4.27	4.02
Water	25.89	25.95	26.00

Figure 2: (a) Training dataset labels repartition (b) Dataset repartition; train, validation and test

layer via cross-attention. Moreover, the global projection vector of shape $[B, 1280]$ is passed through the `added_cond_kwargs['text_embeds']` layers.

Training Process. As shown in the Figure 3, the model learns by noising training data (i.e. VAE Encoder output), through the successive addition of Gaussian noise (forward process). Then the model is used reverse this process (reverse process) to turn noise back into data by removing the noise added during each diffusion step. More specifically, the latent z_t is the output of the VAE encoder from the input image x_t , and noise is added to simulate a step in the forward diffusion process, governed by a scheduler that defines the noise distribution at each t . More specifically, the forward diffusion process, which adds noise to an input data z_0 over T timesteps by adding Gaussian noise, is defined as:

$$z_t = \sqrt{\bar{\alpha}_t} z_0 + \sqrt{1 - \bar{\alpha}_t} \epsilon, \quad \epsilon \sim \mathcal{N}(0, \mathbf{I}) \quad (3)$$

Here, $\bar{\alpha}_t = \prod_{s=1}^t \alpha_s$ denotes the cumulative noise attenuation schedule with $\alpha_t = 1 - \beta_t$. The UNet is trained to predict the

Usage	Text Encoder 1 (CLIP ViT-L)	Text Encoder 2 (OpenCLIP ViT-bigG)
Token-wise embeddings	Yes \rightarrow shape $[B, 77, 768]$	Yes \rightarrow shape $[B, 77, 1280]$
CLS token (global summary of captions)	Not used	Yes \rightarrow shape $[B, 1280]$ (projected afterwards)
Projection (text_projection)	No	Yes (CLS \rightarrow projection \rightarrow text_embeds)

Table 1: Comparison between Text Encoder 1 (CLIP ViT-L) and Text Encoder 2 (OpenCLIP ViT-bigG) in the SDXL architecture.

noise component ϵ added at timestep t , conditioned on both time and prompt embeddings. This enables the model to learn how semantic information influences denoising across different degradation levels.

During training (Figure 4), the model receives a corrupted latent z_t for a randomly sampled timestep $t \in [0, 1000]$ and is tasked with predicting the corresponding ϵ_t . The loss is computed over multiple such noise levels per batch and epoch.

During inference (generation), the process begins from a pure Gaussian noise sample z_T . The UNet iteratively denoises this latent through T steps, each conditioned on the text prompt. Although the model was trained on a schedule of $T = 1000$ steps, it is common in practice to use only 25 to 50 steps for generation. At each step t , the model predicts ϵ_t , and uses the reverse schedule to approximate z_{t-1} . After the final step, the latent z_0 is decoded by the VAE to produce the final image x_0 .

4.2. Training approaches and parameterization

In this study, we compare the effects of two fine-tuning strategies on the main components of the SDXL architecture: the UNet backbone and the two text encoders (TE1 and TE2). The first approach involves *full fine-tuning*, where all model weights are updated. While this allows maximum flexibility and capacity for domain adaptation, it is computationally expensive and increases the risk of overfitting, particularly in scenarios with limited training data.

The second approach uses *Low-Rank Adaptation (LoRA)*, a parameter-efficient fine-tuning method. In this setting, the original model weights are kept frozen, and trainable low-rank matrices are injected into selected layers — typically in the attention and cross-attention modules. These additional parameters allow the model to learn task-specific adaptations with a significantly reduced memory and computational footprint.

Our goal is to evaluate whether LoRA is sufficient for adapting a pretrained latent diffusion model to SAR image generation, and under what conditions full fine-tuning is still required. We hypothesize the following:

- **Full fine-tuning of the UNet** may be necessary to capture the low-level statistical and physical properties that characterize SAR images (e.g., speckle, radiometric contrast, geometry).
- **LoRA-based tuning of the text encoders** may be sufficient, as the semantic embedding space for textual prompts remains relatively stable and may not require extensive retraining across modalities.

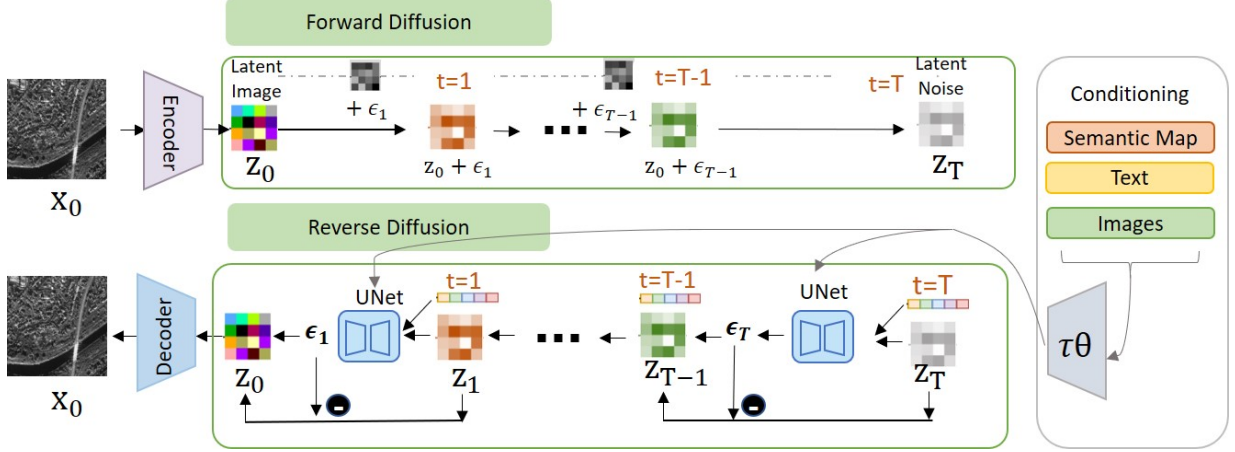


Figure 3: Forward and Reverse Process in Stable Diffusion XL

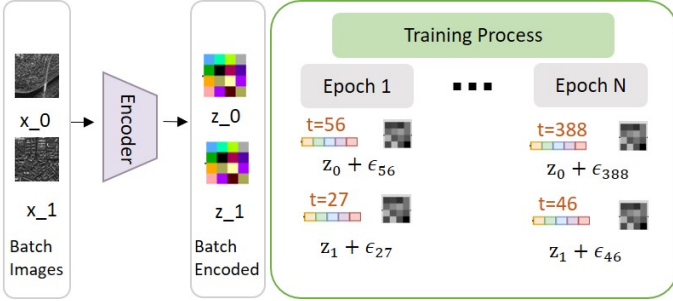


Figure 4: Random timesteps sampling over a batch during training epochs

In Section 5, we empirically evaluate these strategies across several model configurations. We use both semantic and statistical metrics to determine the most effective fine-tuning paradigm for generating realistic and coherent SAR images from textual descriptions.

4.3. Evaluation of generated SAR images

Evaluation Dataset. To assess the realism of the generated SAR images, we use a test dataset composed of triplets: [captions, labels, real SAR images]. Since SAR intensity distributions vary significantly depending on the type of scene, we perform a label-specific evaluation to account for this variability. The labels correspond to semantic scene categories — *forest, field, city, airport, seacoast, port, mountains, beach, industrial, and residential* — derived from a manually created keyword dictionary. For each label, the associated test captions are used as prompts to generate synthetic SAR images. In total, we generate 30 images per label across 11 categories, resulting in 330 generated images used for evaluation and comparison across model configurations.

SAR Statistics analysis. To compare the amplitude distributions between real and generated SAR images, we flatten each image into a one-dimensional array of pixel amplitudes. As described in Section 3, a normalization step is applied during pre-processing, and pixel values are clipped to the range $[0, 1]$, introducing an artificial saturation effect at the upper bound.

To enable accurate statistical comparisons using the Kullback–Leibler (KL) divergence, we first exclude all pixel values strictly above 0.999, corresponding to saturated pixels. We then compute the proportion of saturated pixels separately and renormalize the histograms over the remaining values so that the probability density integrates to 1.

The KL divergence is computed between the empirical amplitude distributions of real and generated images, separately for each semantic category. Given two discrete probability distributions, P (real SAR) and Q (generated SAR), estimated over amplitude bins i , the KL divergence is given by:

$$D_{\text{KL}}(P \parallel Q) = \sum_i P(i) \log \left(\frac{P(i)}{Q(i)} \right) \quad (4)$$

Prompt-Image Alignment. Beyond statistical similarity, we also evaluate how well the generated SAR images align semantically with their conditioning prompts. To this end, we fine-tuned a CLIP ViT-L/14 model, on a separate dataset containing SAR image–caption pairs, using a batch size of 100, with the goal of embedding both modalities into a common latent space adapted to radar imagery.

To quantify alignment, we adopt two complementary evaluation strategies. First, we compute the *ranking score*, which measures how well each image is matched to its correct caption among a set of other texts. For each batch of $N = 16$ image–text pairs, we extract normalized image embeddings $f_{\text{img}}(x_i)$ and text embeddings $f_{\text{text}}(t_j)$, and compute the cosine similarity matrix $S \in \mathbb{R}^{N \times N}$:

$$S_{ij} = \frac{\langle f_{\text{img}}(x_i), f_{\text{text}}(t_j) \rangle}{\|f_{\text{img}}(x_i)\| \cdot \|f_{\text{text}}(t_j)\|} \quad (5)$$

We apply a softmax normalization across each row of the matrix to interpret the values as match probabilities. For each image x_i , we compute the rank r_i of its corresponding ground-truth caption t_i within the list of possible captions. We report the mean rank r_μ , median rank and rank variance r_σ over the evaluation set:

$$r_\mu = \frac{1}{N} \sum_{i=1}^N r_i \quad r_\sigma = \frac{1}{N} \sum_{i=1}^N (r_i - r_\mu)^2 \quad (6)$$

A lower mean rank indicates better semantic alignment between the generated image and its textual prompt.

In addition to ranking-based evaluation, we compute the *cosine similarity* between each generated image and its prompt, using the same fine-tuned SAR CLIP model. For each of the 11 semantic labels, we average these similarity scores across all generated samples to obtain a per-label, per-model alignment metric. The results are presented as heatmaps, where higher values indicate stronger text–image coherence. As a reference baseline, we compute the same similarity scores between real SAR images and their corresponding captions using the same CLIP model. These values are included at the bottom of each heatmap for visual comparison.

This two-pronged evaluation approach allows us to assess both *relative ranking performance* (i.e., how uniquely matched each prompt is to its image) and *absolute similarity* (i.e., how close the embedding vectors are).

SAR Textural Indicators. To evaluate the structural realism of the SAR images generated by our model, we compute textural indicators derived from the Gray-Level Co-occurrence Matrix (GLCM), following the classical method proposed by Haralick et al. [27].

We base this analysis on the same set of 330 labeled real and generated SAR images. From each image, we extract homogeneous patches of size 64×64 pixels, using segmentation masks inferred by the Segment Anything Model (SAM) [28]. Specifically, we identify the largest mask in each image and apply a sliding kernel to extract patches that are fully contained within that region. For each patch, we compute the GLCM.

Given a patch of size (N, N) with gray-level quantized amplitude values, the GLCM is defined as:

$$\text{GLCM}(l, k, \theta, d) = \frac{1}{N_d N_\theta} \sum_{x=1}^M \sum_{y=1}^N \begin{cases} 1, & \text{if } I(x, y) = l \text{ and } I(x + \Delta x, y + \Delta y) = k \\ 0, & \text{otherwise} \end{cases} \quad (7)$$

where $(\Delta x, \Delta y) = (\text{round}(d \cos \theta), \text{round}(d \sin \theta))$, and d and θ denote the distance and orientation of the co-occurrence pair.

From the normalized GLCM, we compute four classical Haralick texture features:

- **Correlation:** $\sum_{l,k} \text{GLCM}(l, k) \frac{(l - \mu_l)(k - \mu_k)}{\sigma_l \sigma_k}$
- **Homogeneity:** $\sum_{l,k} \frac{\text{GLCM}(l, k)}{1 + (l - k)^2}$
- **Contrast:** $\sum_{l,k} \text{GLCM}(l, k) (l - k)^2$
- **Entropy:** $-\sum_{l,k} \text{GLCM}(l, k) \log(\text{GLCM}(l, k) + \epsilon)$

These features characterize various aspects of image texture such as spatial regularity, smoothness, contrast, and randomness. We compute them across multiple orientations θ and distances d to assess rotation-invariant properties.

We then compare the distributions of these indicators between real and generated SAR images across semantic categories

(*forest, city, port*, etc.), analyzing both their mean values and their variation under rotation. This enables us to assess whether the model has captured label-specific structural patterns and preserved the geometric and statistical richness of SAR texture.

5. Experiments and results

In this section, we present a series of experiments conducted using Stable Diffusion XL to evaluate the impact of various fine-tuning configurations. Our goal is to assess the individual contribution of each architectural component (UNet, Text Encoder 1, and Text Encoder 2), and to investigate whether they can be adapted independently or require joint tuning for optimal performance.

All experiments are performed using our custom training dataset of 100,000 SAR image–caption pairs (1024 per 1024 pixels for each image). Training hyperparameters are kept fixed across all configurations to ensure consistency and fair comparison. Specifically, the learning rate is set to $5e-5$ for the UNet and $4e-5$ for both text encoders. These values were chosen based on empirical stability under the available computational budget (one NVIDIA H100 GPU), while fitting within memory constraints.

To promote reproducibility, we use a fixed random seed for all experiments. The training dataset is shuffled identically across configurations, and the same seed is used for image generation (1024 per 1024 pixels) during both training and evaluation. This ensures that differences in results arise solely from the fine-tuning strategy and not from data ordering or sampling variability.

5.1. Importance of the noise offset

When fine-tuning the model on SAR images, we introduce a small noise offset during the forward diffusion process. At each training step, the standard Gaussian noise $\varepsilon \sim \mathcal{N}(0, 1)$ is perturbed by an additional random term, defined as:

$$\varepsilon_{\text{offset}} = \varepsilon + \gamma \delta, \quad \delta \sim \mathcal{N}(0, 1), \quad \gamma = 0.035 \quad (8)$$

This modification effectively shifts the noise distribution to $\mathcal{N}(0, 1 + \gamma^2)$, introducing a variability per sample and per channel without altering the spatial structure of the noise. For SAR imagery, which exhibits heavy-tailed amplitude distributions and pronounced contrast between bright scatterers (e.g., buildings, ships) and low-return regions (e.g., calm water), this additional stochasticity helps the model better capture the full dynamic range.

To evaluate its impact, we compare two training runs with identical LoRA settings on the UNet and both text encoders: *rain-beach-6* (with noise offset) and *umbrella-sand-8* (without noise offset). These configurations differ only in the inclusion of the noise offset.

Train ID	UNet LoRA		TE1 LoRA		TE2 LoRA		Noise Offset	CLIP Rank		KL ↓
	r	a	r	a	r	a		ν	σ	
rain-beach-6	256	128	8	4	8	4	✓	2.34	3.73	0.17
umbrella-sand-8	256	128	8	4	8	4	✗	2.54	4.40	1.16

Table 2: Comparison of trainings - at epoch 8 - with and without noise offset and LoRA (r: rank, a: alpha).

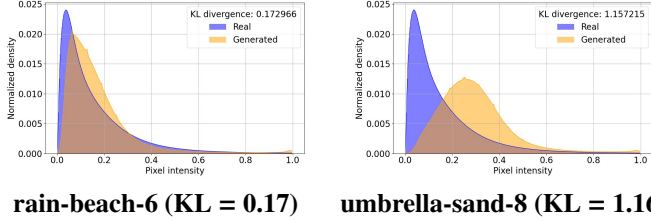


Figure 5: Comparison of KL distances probability density distribution between 330 real and generated flattened images, with and without noise offset

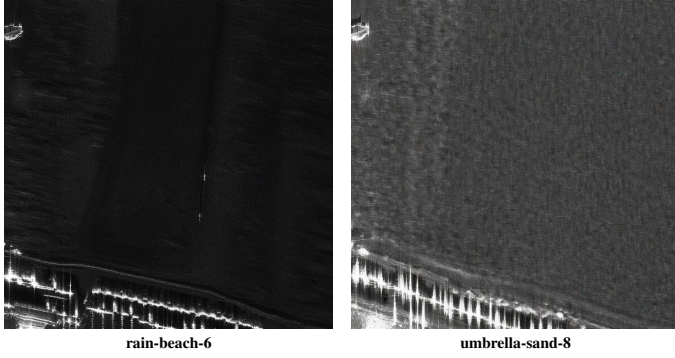


Figure 6: Comparison of image generated during training - at epoch 8 - with the same prompt: "A satellite view of a port with a boat in the water and a forest nearby." (see more examples in Appendix Appendix A.2)

As illustrated in Figure 6, the absence of a noise offset leads to lower-contrast images with dull gray tones, failing to reproduce key SAR-specific features—such as the strong reflectivity contrast between land and sea. In contrast, introducing a small noise offset improves dynamic range modeling and enhances the physical realism of textures, as reflected by both visual inspection and the significant drop in KL divergence (Table 2). Based on these results, we apply a noise offset by default in all subsequent training runs.

5.2. Study on the UNet, TE1 and TE2

In this experiment, we compare different fine-tuning strategies for each major module of the SDXL architecture, namely, the UNet backbone, Text Encoder 1 (TE1), and Text Encoder 2 (TE2), to assess their relative importance and degree of independence. Each module is either fully fine-tuned (i.e., all weights are updated) or fine-tuned using Low-Rank Adaptation (LoRA) adapters.

By default, LoRA adapters are applied to the attention projection layers of the UNet: $[q_{proj}, k_{proj}, v_{proj}, out_{proj}]$. For the text

encoders, LoRA is also applied to the same types of projection layers. Current libraries do not support LoRA on normalization layers; however, for the configuration identified as *super-bowl-2*, we include additional convolutional LoRA adapters in layers $[to_q, to_k, to_v, to_{out}, 0]$ as well as convolutional layers $[conv_1, conv_2]$ to analyze the contribution of convolutions to generative performance.

Train ID	UNet LoRA		TE1 LoRA		TE2 LoRA		CLIP Rank		KL ↓
	r	a	r	a	r	a	ν	σ	
lake-mont-9	F	F	*	*	*	*	1.84	2.07	0.53
soleil-up-7	F	F	8	4	8	4	1.61	1.17	0.42
mummy-pen-8	F	F	F	F	F	F	2.19	3.62	1.78
eau-vie-4	256	128	F	F	F	F	2.34	3.77	1.15
smile-road-5	256	128	8	4	F	F	2.77	5.49	0.032
rain-beach-6	256	128	8	4	8	4	2.34	3.73	1.17
king-kong-9	256	128	F	F	8	4	2.44	4.24	1.13
super-bowl-2	256	128	8	4	8	4	2.32	3.78	0.49

Table 3: Comparison of training configurations - at epoch 8 - with UNet (F: all weights, *: weights freed) and Text Encoders with LoRA (r: rank and a: alpha).

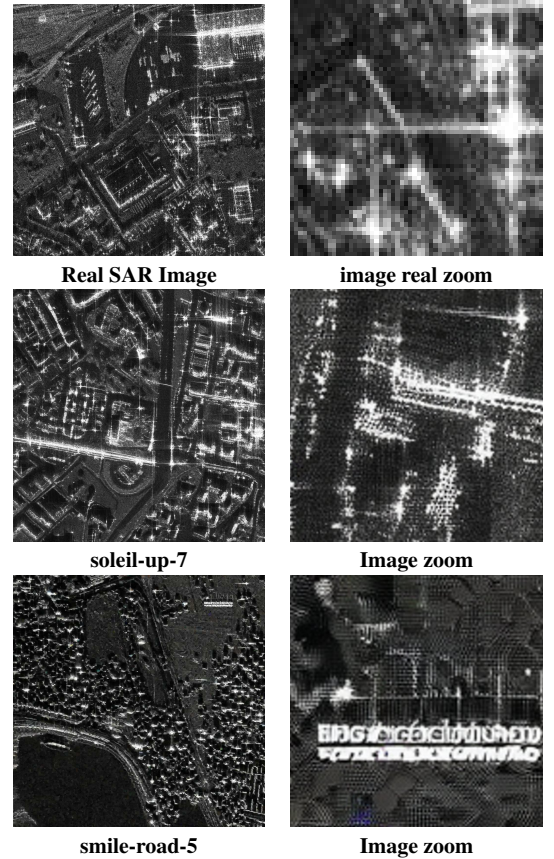


Figure 7: Comparison of image real and generated - at epoch 8 - with the same prompt: "A satellite view of a dynamic city with several buildings and a network of roads."

As shown in Table 3, full fine-tuning of the UNet consistently improves alignment and realism, as reflected in lower CLIP rank

mean and variance. Although the model *smile-road-5* achieves the best KL divergence score—indicating good statistical similarity to real SAR distributions—its high rank variance and weak alignment suggest instability. Indeed, visual inspection (Figure 7) reveals that this model sometimes generates unrealistic features, such as distorted textures or handwritten-like artifacts, which do not match the prompt.

In contrast, the model *soleil-up-7* delivers both low CLIP rank and strong visual coherence. This configuration uses full UNet fine-tuning combined with LoRA on both text encoders, preserving prompt alignment while allowing the network to learn SAR-specific spatial patterns. Additional examples are shown in Appendix Appendix A.2, Figure A.18.

To better understand which parts of the UNet contribute most to learning, we analyze the magnitude of parameter updates relative to the pretrained weights. As shown in Appendix Appendix A.1 (Figure A.17), the largest changes are observed in the first ResNet blocks of the downsampling path and the final layers of the upsampling path. This suggests that early convolutional layers are critical for encoding SAR-specific noise and structure, further justifying the need for full fine-tuning of the UNet.

5.3. Study on LoRA Rank and Alpha

In this section, we investigate the impact of varying LoRA rank and scaling factor (*alpha*) on the performance of the fine-tuned model. All configurations use full fine-tuning of the UNet (F), while LoRA is applied to both text encoders (TE1 and TE2) with different rank–alpha pairs. Results are summarized in Table 4.

Train ID	UNet	TE1 LoRA		TE2 LoRA		CLIP Rank		KL ↓
		r	a	r	a	ν	σ	
soleil-up-7	F	8	4	8	4	1.61	1.17	0.42
apple-color-6	F	64	32	64	32	1.74	1.77	0.37
fiber-network-6	F	128	64	128	64	1.77	1.59	0.42
screen-light-4	F	256	128	256	128	1.70	1.65	0.37

Table 4: Comparison of LoRA configurations – at epoch 8 – for Text Encoders 1 and 2 (r: rank and a: alpha) and UNet full fine-tuning (F).

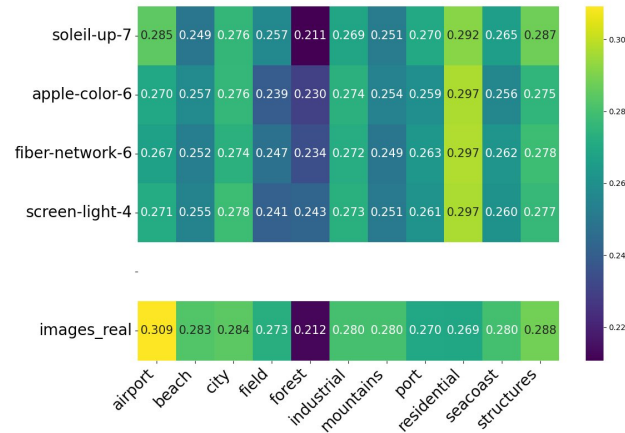


Figure 8: Mean cosine distance between image-text pairs, compared to real ones.

Contrary to what has been observed in other domains, our results suggest that increasing the LoRA rank and alpha beyond moderate values does not improve vision–language alignment in the SAR generation setting. As shown in Table 4, the best CLIP alignment metrics (lowest rank mean and variance) are achieved with relatively low-rank settings ($r = 8$, $\alpha = 4$), as used in the *soleil-up-7* model. Larger ranks, such as those in *fiber-network-6* and *screen-light-4*, lead to slightly degraded alignment scores despite similar KL divergence.

Figure 8 further confirms this: the cosine similarities between image–prompt pairs for *soleil-up-7* are closer to those observed between real SAR images and their captions, indicating more faithful semantic representation. In contrast, higher LoRA configurations tend to blur category separability, possibly due to overfitting or excessive parameter capacity in the text encoders.

These results suggest that compact LoRA adapters (with low rank and scaling) are sufficient for prompt–image alignment in this domain and may generalize better than overparameterized configurations.

5.4. Study on Batch Size

In our dataset, SAR images exhibit considerable variability in contrast due to differences in scene content and acquisition conditions. For instance, forested areas may appear brighter when wet, such as after rainfall or when near water bodies. Agricultural fields show distinct backscatter signatures depending on crop type, growth stage, or soil moisture. Urban regions also vary depending on building materials and orientation. This intrinsic variability presents challenges in modeling consistent textural and radiometric patterns.

To mitigate overfitting to the amplitude distribution of small batches and promote better generalization across diverse SAR characteristics, we investigate the impact of batch size on model performance. Larger batches are expected to provide more statistically representative samples within each optimization step. Due to hardware limitations, we simulate larger batch sizes using gradient accumulation. Results are presented in Table 5.

As shown in Table 5 and Figure 9, increasing the batch size generally improves the similarity between generated and real SAR distributions, as measured by the KL divergence. Larger batches expose the model to a broader diversity of textures and amplitude statistics, helping it learn more robust and representative features. The best KL score is observed for the 64-image configuration, suggesting a potential trade-off: extremely large batches (e.g., 128) may lead to diminishing returns or underfitting, while mid-sized batches offer an optimal balance between generalization and convergence.

5.5. Study on VAE Decoder

While most studies using SDXL retain the original Variational Autoencoder (VAE) without modification, we hypothesize that fine-tuning its encoder and/or decoder components may improve latent representation quality for SAR images. This is motivated by the fact that SAR data differ significantly from natural images in terms of statistical structure, noise characteristics (e.g., speckle), and semantic content.

Train ID	UNet	TE1		TE2		Batch Size	CLIP Rank		KL ↓
		r	a	r	a		ν	σ	
soleil-up-7	F	8	4	8	4	16	1.61	1.17	0.43
king-elephant-9	F	8	4	8	4	32	1.63	1.05	0.42
whale-north-8	F	8	4	8	4	64	1.79	1.48	0.35
boad-see-9	F	8	4	8	4	128	1.79	1.45	0.42

Table 5: Comparison of batch size at epoch 8 with a fixed training configuration (UNet full fine-tuning **F**, LoRA for Text Encoders).

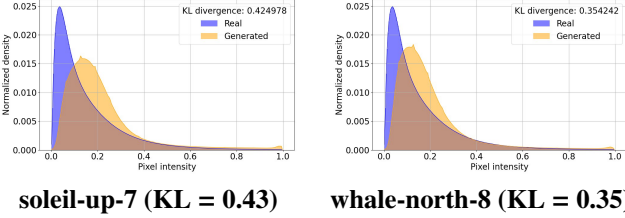


Figure 9: Comparison of KL distance distributions between 330 real and generated flattened images.

Fine-tuning the SDXL VAE, however, proves particularly challenging when transferring to a new domain such as SAR. In our experiments, fine-tuning the VAE encoder often led to latent space instability and mode collapse. In practice, the pretrained VAE already reconstructs SAR images with low error, and the decoded outputs follow a Rayleigh-like amplitude distribution that closely resembles real SAR data. Attempts to adjust the encoder disrupted this alignment and led to overfitting.

Moreover, training separately of the VAE from the rest of the model (UNet and text encoders) proved to be ineffective, because coherence across components is essential in foundation model pipelines. To address this, we chose to fine-tune only the VAE decoder jointly with the UNet and both text encoders during a final refinement phase.

Despite the VAE’s strong reconstruction ability in pixel space, generating SAR images from pure Gaussian noise during inference remains challenging. While UNet fine-tuning helps, the decoder often fails to fully reproduce the sharp textures and amplitude dynamics typical of SAR data.

To mitigate this, we performed a short refinement training of the decoder (along with the UNet and text encoders)

$$z_0 = \frac{1}{\sqrt{\bar{\alpha}_t}} (\hat{z}_t - \sqrt{1 - \bar{\alpha}_t} \cdot \epsilon) \quad (9)$$

where $\bar{\alpha}_t$ is the cumulative product of noise schedule coefficients up to timestep t . The resulting z_0 is decoded into a synthetic SAR amplitude image \hat{x} via the VAE decoder.

To ensure that \hat{x} approximates real SAR distributions, we include a KL divergence term comparing the pixel amplitude histograms of \hat{x} and the ground-truth image x :

$$\mathcal{L}_{KL} = D_{KL}(P_{\text{real}}(x) \parallel P_{\text{gen}}(\hat{x})) \quad (10)$$

The total loss used for decoder fine-tuning is:

$$\mathcal{L}_{\text{total}} = \mathcal{L}_{\text{Rayleigh}} + \mathcal{L}_{KL}$$

This formulation encourages the decoder to better approximate SAR-specific amplitude statistics during generation.

Train ID	UNet	VAE		TE1		TE2		CLIP Rank		KL ↓
		E	D	r	a	r	a	ν	σ	
whale-north-8	F	✗	✗	8	4	8	4	1.79	1.48	0.35
whale-north-8-refined	*	✗	✓	8	4	8	4	1.79	1.82	0.33

Table 6: Study on VAE Decoder fine-tuning — with UNet full fine-tuning (**F**) and fixed LoRA for both Text Encoders.

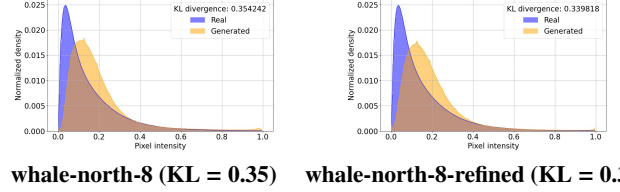


Figure 10: Comparison of KL distance distributions between 330 real and generated flattened images - with 833 refining training steps - with 40 timesteps with 15 timesteps on the last 15 % of the denoising process.

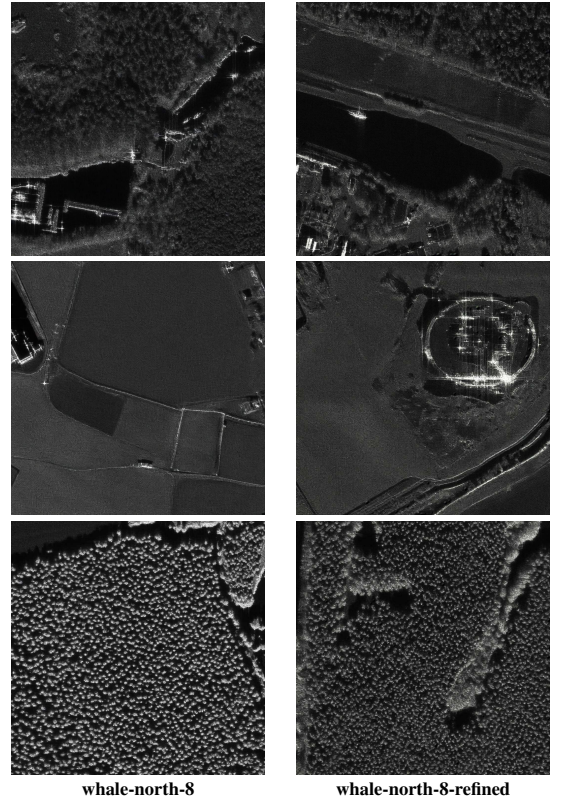


Figure 11: Comparison of generated images — at epoch 8 — with the same prompts: (1) "A satellite view of a port with a boat in the water and a forest nearby." (2) "A satellite view of a vast expanse of land with a circular structure and a few isolated buildings." (3) "A satellite view of a dense forest with a river in the center of the forest."

Overall, we observe that the model **whale-north-8-refined** yields better semantic coherence and finer structural details. As illustrated in Figure 11, it successfully adds a boat to the harbor,

generate a circular structure in an open field, and delineates a river through the center of a forest — all in accordance with the textual prompts. The decoder was refined over 833 steps (equivalent to one epoch), limited intentionally to avoid latent space collapse, which had previously manifested as color artifacts in the generated SAR images. Thus, training the VAE remains delicate, as even minor instabilities can propagate to the generation process and degrade structural or statistical fidelity.

5.6. Study on <SAR> Token Embedding Learning

To improve the model’s transferability to the SAR domain, we adopt a token embedding learning strategy inspired by textual inversion. Instead of relying solely on full model fine-tuning, we introduce a new learnable token <SAR> whose embedding is optimized jointly with the model weights.

During training, we modify the prompts by replacing general descriptions like “A satellite view of...” with SAR-specific expressions such as “A <SAR> image of...”. This encourages the model to associate the <SAR> token with the statistical and structural patterns specific to radar imagery. The embedding is updated through backpropagation along with the UNet, aligning the textual representation with SAR-specific latent visual features.

Train ID	UNet	VAE		TE1 LoRA		TE2 LoRA		CLIP Rank		KL ↓
		E	D	r	a	r	a	ν	σ	
whale-north-8	F	✗	✗	8	4	8	4	1.79	1.48	0.35
tour-reine-2	F	✗	✓	8	4	8	4	1.74	1.35	0.34
heart-rose-2	F	✗	✓	8	4	8	4	1.68	1.31	0.23

Table 7: Study on <SAR> Token Embedding Learning — with UNet full fine-tuning (F) and fixed LoRA for both Text Encoders.

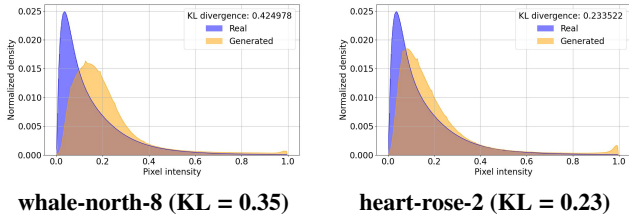


Figure 12: Comparison of KL distance distributions between 330 real and generated flattened images.

The model *heart-rose-2* achieves the lowest KL divergence (0.23) and optimal CLIP Rank scores (1.68 and 1.31 for ν and σ , respectively), indicating superior performance in generating realistic SAR images (Table 7). Histogram comparison (Figure 12) reveals that the probability density distribution of heart-rose-2 more closely captures the inherent dynamics of SAR data, indicating that this model learns better representational dynamics of Synthetic Aperture Radar imagery.

Given the class imbalance in our dataset (e.g., Forest, Airport, City, etc.), combined with the fact that SAR images have distinct distribution dynamics depending on the observed scene, we further evaluated model behavior per semantic category:

Category	whale-north-8			heart-rose-2		
	CLIP Rank		KL ↓	CLIP Rank		KL ↓
	ν	σ		ν	σ	
Forest	2.27	1.80	1.30	1.77	0.65	1.23
City	1.73	1.60	0.35	1.37	0.37	0.23
Field	2.37	2.50	0.17	2.07	1.60	0.16
Port	2.20	1.89	1.02	2.60	4.97	0.42
Airport	2.37	3.03	0.18	2.27	2.80	0.16
Mountains	2.47	3.32	0.73	1.73	1.53	0.28
Structures	2.50	3.05	0.30	2.60	3.57	0.24
Seacoast	2.57	3.65	0.36	1.57	0.65	0.31
Beach	1.97	2.43	0.31	1.97	2.70	0.24
Industrial	1.93	1.60	0.23	2.00	2.00	0.22
Residential	1.43	0.51	0.14	1.40	0.84	0.08

Table 8: Per-category CLIP Rank statistics (ν , σ) and KL divergence for the models *whale-north-8* and *heart-rose-2*.

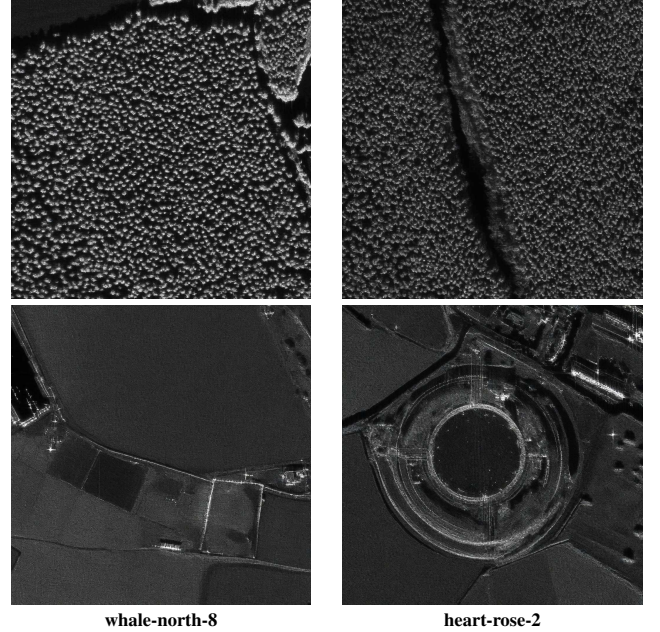


Figure 13: Comparison of generated images — at epoch 8 — with the same prompts: (1) “A SAR image of a dense forest with a river in the center of the forest.” (2) “A SAR image of a vast expanse of land with a circular structure and a few isolated buildings.”

As shown in Table 8, the *heart-rose-2* model outperforms *whale-north-8* across nearly all categories, especially in forested, mountainous, and seacoast scenes — which typically exhibit more complex scattering patterns. Notably, it is capable of composing scenes that were never explicitly observed during training like “a circular structure in a city center” or “a river in the middle of a dense forest” (Figure 13). In general, *heart-rose-2* generates high-quality SAR images with realistic spatial structures and texture patterns, as illustrated in Figure A.20 (see Appendix Appendix A.3).

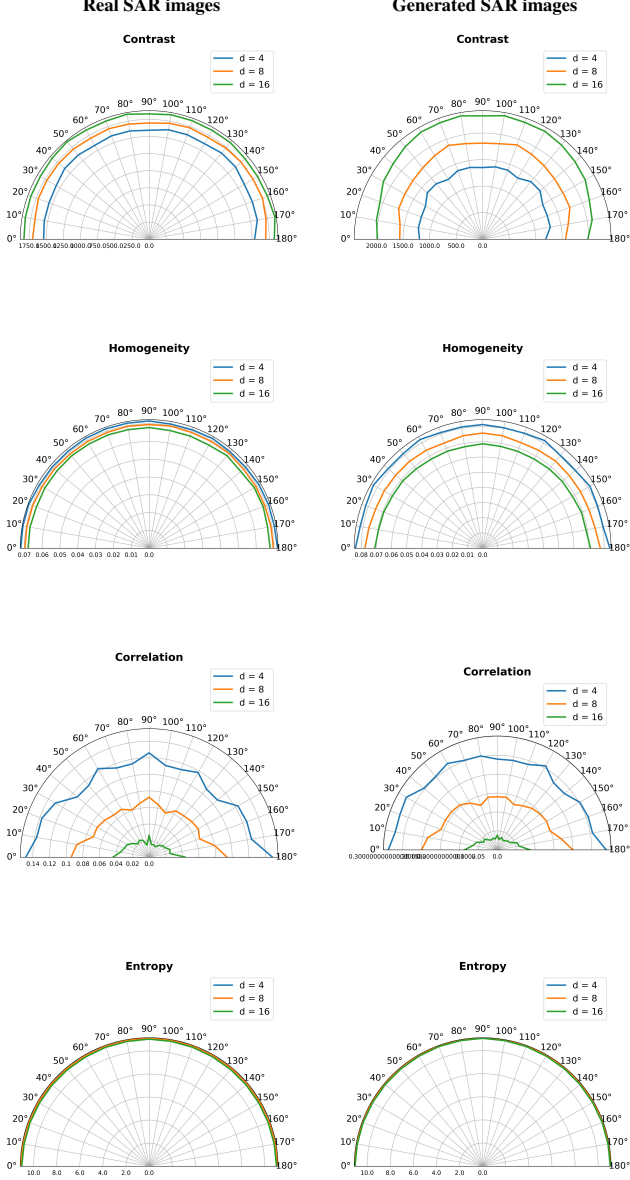


Figure 14: GLCM texture metrics (epoch 10) for real vs generated SAR images at different distances and rotation angles. Each row shows one metric: contrast, homogeneity, correlation, and entropy.

As detailed in Section 4.3, GLCM-based texture metrics provide further evidence of generative realism. Figure 14 shows that the model effectively reproduces directional patterns for contrast, entropy, and homogeneity. However, deviations remain in the correlation metric, especially at certain angles, suggesting that the model may not fully capture the spatial dependencies induced by SAR imaging geometry or coherent scattering mechanisms.

6. Applications

Our fine-tuned Stable Diffusion XL model for SAR imagery can be used in several practical applications. One of its key

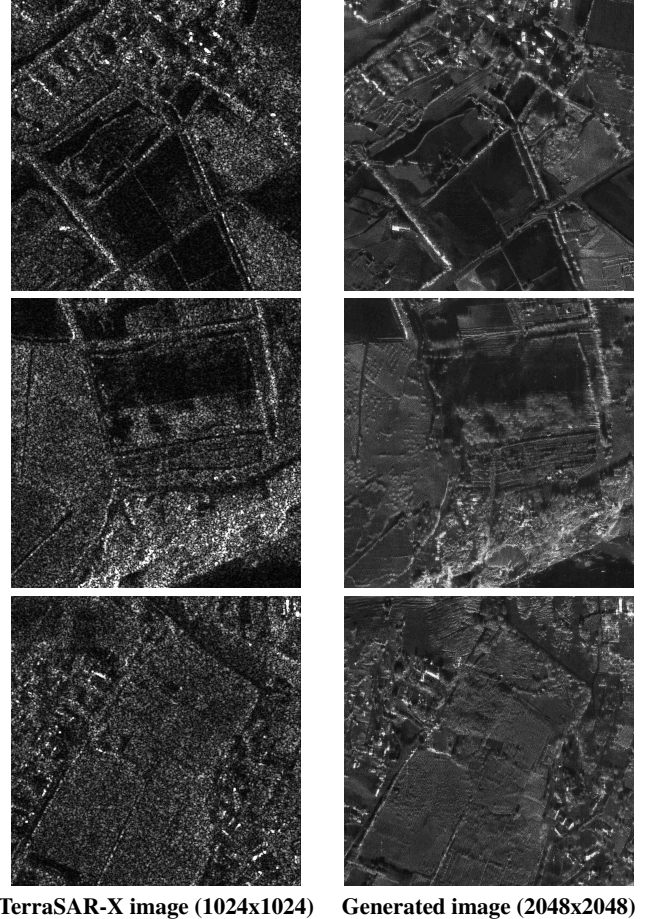
strengths lies in its ability to perform image-to-image generation while preserving essential statistical properties of SAR data, such as speckle texture and reflectivity distributions. This makes it particularly useful for denoising, adding spatial detail, or enhancing outputs from ONERA’s physics-based simulators.

In previous work, we demonstrated the effectiveness of our early fine-tuned model in a conditional, multi-resolution ControlNet pipeline for large-scale scene generation [29]. We also showed its ability to transform satellite TerraSAR-X data into high-resolution, airborne-like imagery with reduced sensor noise [30]. These applications rely on ControlNet to guide generation using structural priors.

Here, we illustrate two new use cases: enhancing real SAR images and improving synthetic outputs from physics-based simulators.

6.1. Enhancing TerraSAR-X image at 40cm

We use our model to enhance TerraSAR-X satellite acquisitions. The original images (acquired at 1.35 m resolution) are up-sampled to 40 cm in the frequency domain and passed through our generation pipeline.



TerraSAR-X image (1024x1024) Generated image (2048x2048)

Figure 15: Enhancing TerraSAR-X images with prompts (1): "A SAR image of various patches of crop fields with roads and a cluster of houses.", (2): "A SAR image a large rectangular field near a beach." and (3): "A SAR various patches of fields with vegetation and a few houses."

As shown in Figure 15, the enhanced images exhibit sharper textures, improved contrast, and more homogeneous noise characteristics compared to the original TerraSAR-X inputs, while preserving realistic backscattering structures. In particular, the TerraSAR-X reference image at a resolution of around 1 m contains characteristic speckle patterns on which the model can diffuse to add realistic high-frequency detail.

6.2. Enhancing physics-based simulator image: subsampled from 80cm to 40cm

We also apply our model to improve the realism of synthetic SAR images generated by ONERA’s EMPRISE simulator. These images are enhanced to include finer textures and more realistic spatial structure.

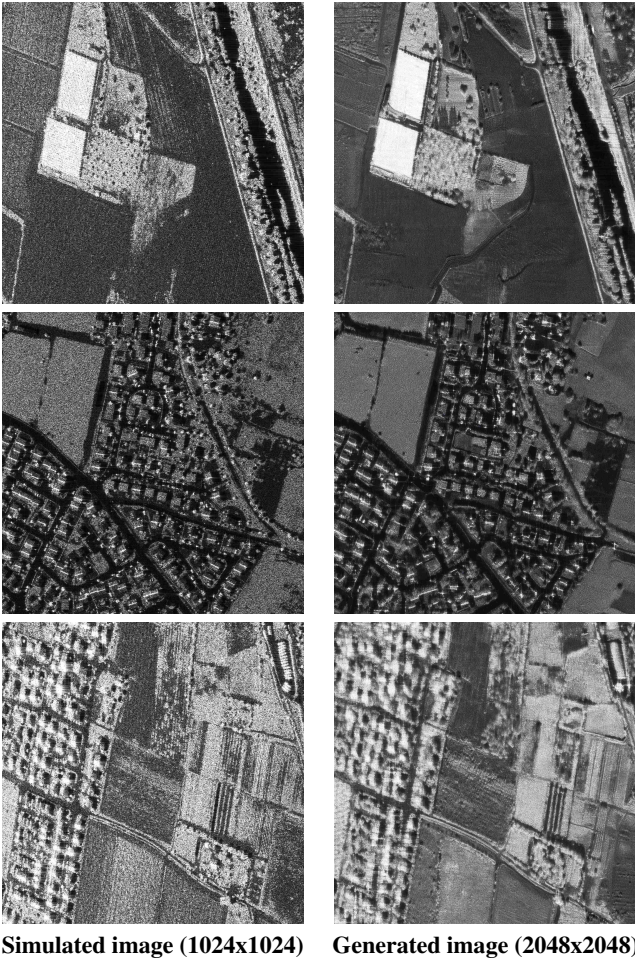


Figure 16: Enhancing ONERA’s physics-based simulator EMPRISE Images with prompts (1): "A SAR image of distinct patches of crop fields near a long river.", (2): "A SAR image of a dynamic city with buildings near highways and a few isolated fields." and (3): "A SAR image with crop fields near a city."

Figure 16 highlights the model’s ability to enhance simulated SAR images by adding spatially consistent fine textures, making them visually closer to real data and more suitable for human interpretation. In particular, it enriches vegetated areas with realistic structural details and interprets ambiguous shadow regions by adding plausible vegetation patterns.

7. Discussion and Conclusion

This work is, to our knowledge, the first comparison study of fine-tuning techniques on a large-scale latent diffusion model — Stable Diffusion XL (SDXL) for a radically different imaging modality: Synthetic Aperture Radar (SAR). While most existing research focuses on generative adaptation for natural images (optical, RGB, photorealistic domains), we show that it is possible to adapt a vision-language foundation model to generate physically grounded, speckle-heavy SAR data. This contribution goes beyond SAR itself: it opens up new possibilities for adapting foundation models to other underrepresented sensing domains such as hyperspectral, infrared, depth, or medical imaging.

By exploring multiple fine-tuning strategies—full UNet updates, Low-Rank Adaptation (LoRA) for text encoders, token embedding learning, and VAE decoder refinement, we provide a reproducible framework to adapt large pretrained diffusion models to unseen imaging physics. We further propose evaluation tools specific to SAR, including statistical distance metrics (KL divergence), structural indicators (GLCM features), and a vision-language alignment score based on a CLIP model fine-tuned for SAR.

However, adapting SDXL to SAR comes with key challenges. First, the statistical and visual properties of SAR data are fundamentally different from natural images: they are grayscale, noisy (speckle), anisotropic, and heavily dependent on acquisition geometry. Foundation models pretrained on optical data tend to favor smooth textures, uniform lighting, and naturalistic shapes — biases that can degrade realism in generated SAR samples.

Second, our dataset, although sizeable (100K image-caption pairs), remains imbalanced. Some scene types (e.g., forest or water) dominate the distribution, while others (e.g., airport or industrial zones) are underrepresented, making fine-tuning harder. Furthermore, since SAR lacks direct semantic interpretation, we rely on captions generated from optical counterparts using CogVLM2. While this provides rich textual supervision, it introduces hallucinations due to mismatched spatial coordinates between optical and SAR images.

Normalization is another open issue. We scaled SAR amplitudes to $[0,1]$ using a clipping strategy that introduced an artificial saturation peak, which complicates the generative process. This calls for more principled pre-processing methods that preserve SAR-specific statistics, such as using phase and frequency-domain data, or learning from complex-valued representations directly.

Evaluation of SAR generation remains a bottleneck. Conventional metrics like FID and CLIP score are inadequate for SAR due to their optical training biases. Although we fine-tuned a CLIP model on SAR-caption data, assessing realism and structure fidelity is still difficult without standardized benchmarks or human-perceptual baselines tailored to SAR data.

Despite these limitations, our experiments demonstrate that:

- Full UNet fine-tuning outperforms LoRA-only approaches in capturing SAR-specific structures.

- Embedding a learned token like <SAR> improves semantic alignment and generation quality.
- Fine-tuning the VAE decoder — limited to later timesteps in the reverse diffusion — enhances textural realism without destabilizing the latent space.
- Generated samples can successfully enhance real satellite or simulated SAR images, suggesting practical use for denoising, simulation refinement, and data augmentation.

In summary, this work sets a precedent for adapting pre-trained generative models to unconventional data domains. It delivers insights for both the SAR and broader AI communities on how to transfer powerful foundation models to non-optical, physics-driven settings. Future directions include: multimodal conditioning (e.g., combining text with elevation or optical inputs), learning in the complex SAR domain (amplitude + phase), and developing SAR - native perceptual metrics to better capture realism, structure, and semantic consistency.

Appendix A. Appendix

Appendix A.1. Mean Absolute Weight Change (MAWC)

We defined the Mean Absolute Weight Change (MAWC) as a metric that measures how much the weights of a model have changed between two checkpoints. Unlike metrics that simply count modified weights, MAWC also accounts for the magnitude of change.

Definition.. Let $w_i^{(0)}$ and $w_i^{(1)}$ denote the value of the i -th weight respectively, before and after fine-tuning. Let W be the total number of weights in a given layer.

We define the absolute change in the i -th weight as:

$$\Delta w_i = |w_i^{(1)} - w_i^{(0)}| \quad (\text{A.1})$$

Then, the **Mean Absolute Weight Change (MAWC)** is the average absolute change across all weights:

$$\text{MAWC} = \frac{1}{W} \sum_{i=1}^W \Delta w_i \quad (\text{A.2})$$

To analyze architectural patterns, we compute the MAWC for each layer individually and then report the mean across all layers belonging to the same sub-block (e.g., ResNet 1, Attention 0).

Appendix A.2. Training images generation

To visually assess the quality and diversity of generations, we display side-by-side image samples produced by each model across six representative scene categories.

In Figures A.18 and A.19, we generate images for each model with the same evaluation seed at epoch 8. Furthermore, Stable Diffusion XL behaves deterministically under fixed random seeds and identical training configurations, enabling controlled comparative experiments. We also use the same training seed to ensure that only the configuration changes across experiments. We use several prompts to generate our evaluation images as follows:

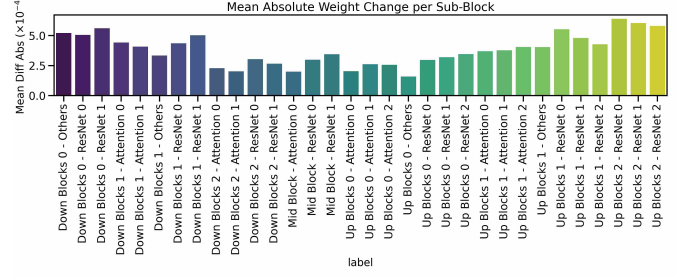


Figure A.17: Mean Absolute Weight Difference per block and sub-block of the UNet during the training configuration *soleil-up-7* with a resolution threshold of 5×10^{-4}

- **Airport:** "A satellite view of an expansive airport with multiple runways, parked aircraft, terminal buildings, parking areas, and surrounding roads."
- **Seacoast:** "A satellite view of a coastal area with a structured marina housing numerous boats, adjacent to a town with organized roadways, and bordered by a sandy beach."
- **Forest:** "A satellite view of a landscape divided into two contrasting areas: a dense forest with a uniform canopy and a barren, plowed field with linear patterns. A winding road cuts through the terrain, connecting the two regions."
- **City:** "A satellite view of a dense urban area with a mix of residential and commercial buildings, winding roads, patches of greenery, and a few large parking lots."
- **Field:** "A satellite view of a vast agricultural landscape with meticulously organized rectangular fields, a winding canal, and a few isolated structures."
- **Mountains/Relief:** "A satellite view of a juxtaposition of rugged mountainous terrain with patches of greenery, and a densely populated urban area with structured roadways, buildings, and swimming pools."

Appendix A.3. Best model images generation

The images shown in Figure A.20 were generated using our best-performing model, **heart-rose-2**. The corresponding prompts used for each image are listed below. (a) "A SAR image of a vast landscape with a rectangular structure in an airport surrounded by roads and patches of vegetation."

(b) "A SAR image of a coastal town with rooftops, a winding road, a sandy beach, boats on the water, and a rocky outcrop."

(c) "A SAR image of a port with a boat in the water and a forest nearby."

(d) "A SAR image of a verdant landscape divided into geometrically patterned fields, a forested area, and a cluster of isolated buildings."

(e) "A SAR image of a vast landscape dominated by meticulously organized agricultural fields, intersected by winding roads, and anchored by a sizable building complex surrounded by vegetation."

(f) "A SAR image of a juxtaposition of organized residential

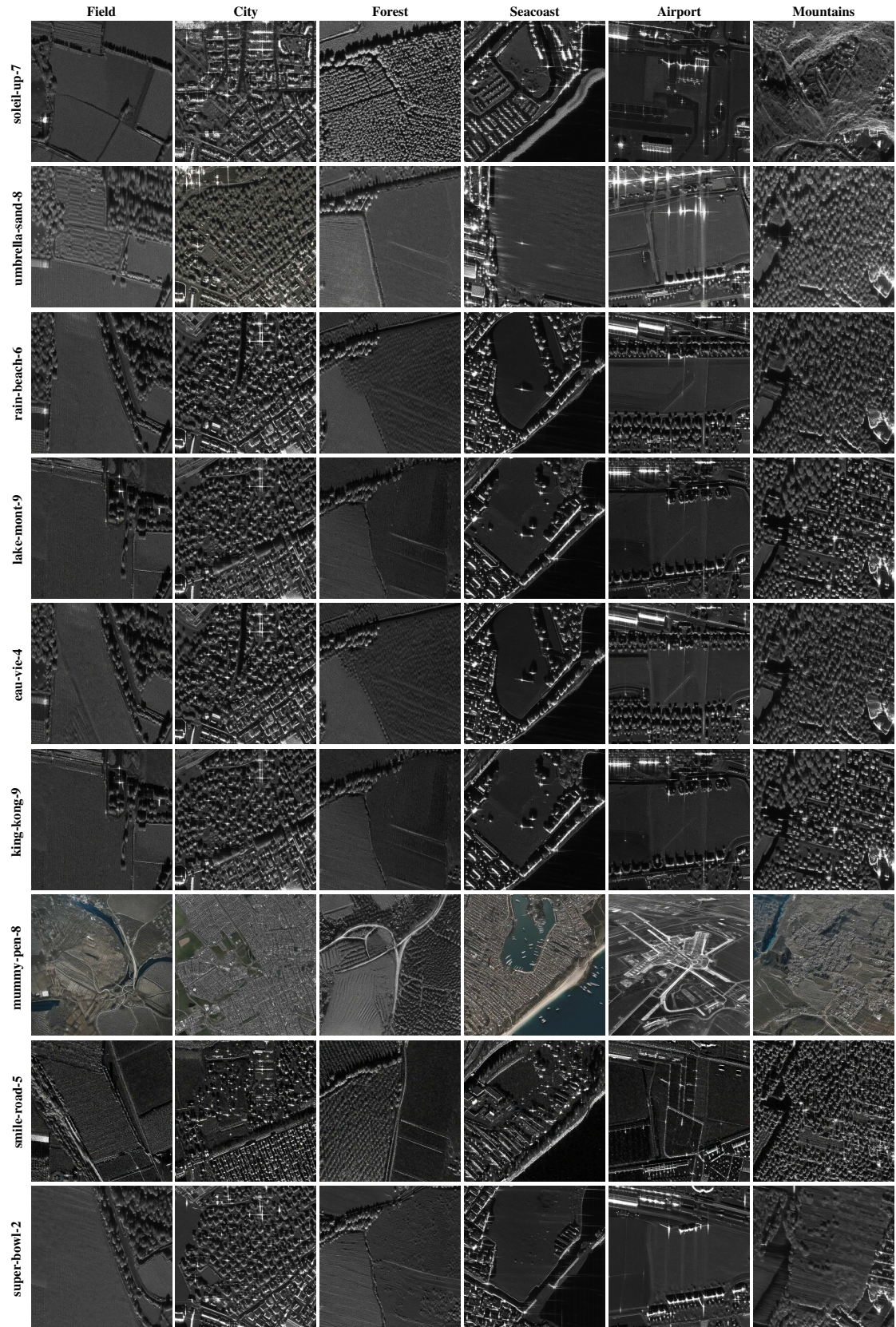


Figure A.18: Study on the UNet, TE1 and TE2: Generated images (1024 per 1024 pixels) per category for 9 different models at epoch 8 (same seed training and evaluation)

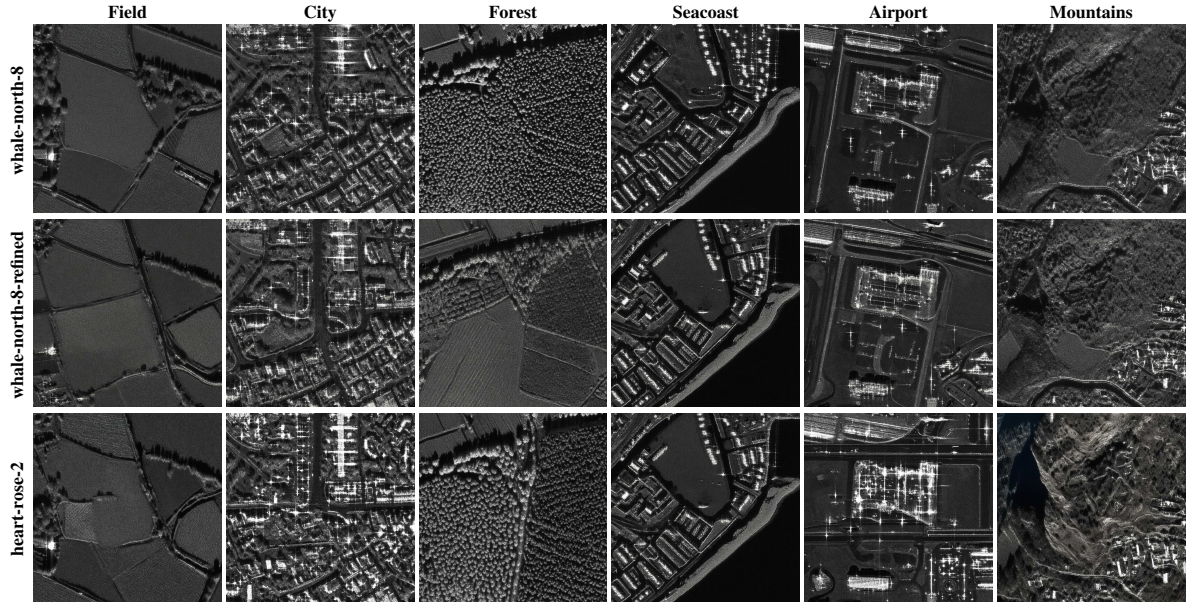


Figure A.19: Refining with VAE vs <SAR> Embedding Learning: Generated images (1024 per 1024 pixels) per category for 9 different models (same seed training and evaluation)

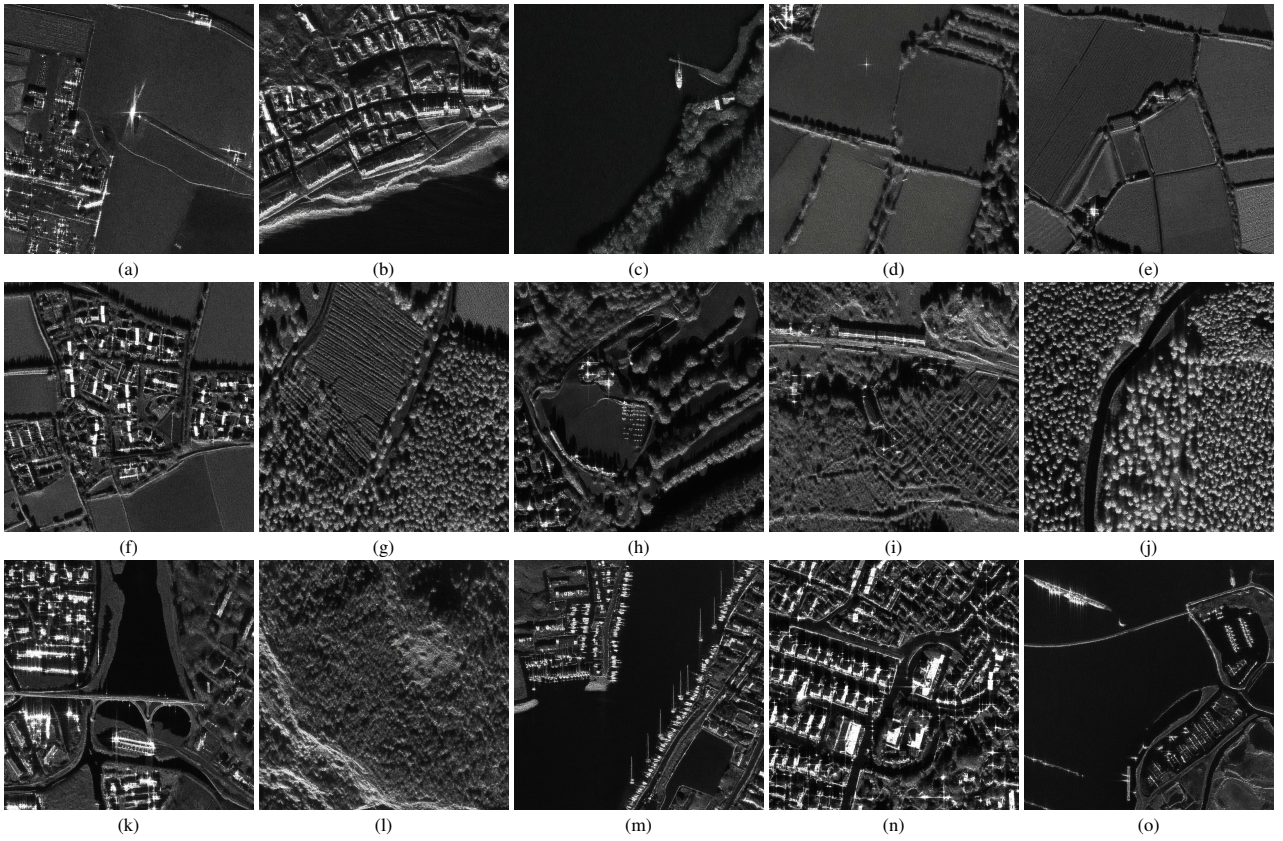


Figure A.20: Generated images (1024 per 1024 pixels) from the **heart-rose-2** model. Each image corresponds to a distinct textual prompt.

areas with pools and vegetation, surrounded by meticulously arranged agricultural fields."

(g) "A SAR image of a dense forest, an agricultural field with linear patterns, a paved road intersecting the field."

(h) "A SAR image of a landscape dominated by agricultural fields, a road, a cluster of buildings, and a solar panel array."

(i) "A SAR image of a hilly terrain with patches of vegetation, a winding road, and scattered structures, possibly residential or agricultural buildings."

(j) "A SAR image of a landscape divided into two areas of dense forest with a uniform canopy. A winding road cuts through the terrain, connecting the two regions."

(k) "A SAR image of a river with a bridge, a town with buildings, roads, and green spaces, and a facility with circular structures."

(l) "A SAR image of a mountainous terrain with a mix of dense forested areas and barren patches. There are visible erosion patterns, possibly from water flow."

(m) "A SAR image of a coastal area with a structured marina housing numerous boats, adjacent to a town with organized roadways, and a large body of water extending to the horizon."

(n) "A SAR image of a residential area with organized streets, houses with varying roof designs, patches of greenery, swimming pools, and a few larger structures that could be commercial or community buildings."

(o) "A SAR image of a large water body with circular patterns, a curving road, a cluster of buildings, and a marina with boats."

References

- [1] J. Yu, Z. Wang, V. Vasudevan, L. Yeung, M. Seyedhosseini, Y. Wu, Coca: Contrastive captioners are image-text foundation models (2022). [arXiv:2205.01917](https://arxiv.org/abs/2205.01917). URL <https://arxiv.org/abs/2205.01917>
- [2] C. Team, Chameleon: Mixed-modal early-fusion foundation models (2025). [arXiv:2405.09818](https://arxiv.org/abs/2405.09818). URL <https://arxiv.org/abs/2405.09818>
- [3] R. Rombach, A. Blattmann, D. Lorenz, P. Esser, B. Ommer, High-resolution image synthesis with latent diffusion models (2022). [arXiv:2112.10752](https://arxiv.org/abs/2112.10752). URL <https://arxiv.org/abs/2112.10752>
- [4] B. F. Labs, Flux, <https://github.com/black-forest-labs/flux> (2024).
- [5] C. Saharia, W. Chan, S. Saxena, L. Li, J. Whang, E. Denton, S. K. S. Ghasemipour, B. K. Ayan, S. S. Mahdavi, R. G. Lopes, T. Salimans, J. Ho, D. J. Fleet, M. Norouzi, Photorealistic text-to-image diffusion models with deep language understanding (2022). [arXiv:2205.11487](https://arxiv.org/abs/2205.11487). URL <https://arxiv.org/abs/2205.11487>
- [6] L. Yu, B. Shi, R. Pasunuru, B. Muller, O. Golovneva, T. Wang, A. Babu, B. Tang, B. Karrer, S. Sheynin, C. Ross, A. Polyak, R. Howes, V. Sharma, P. Xu, H. Tamoyan, O. Ashual, U. Singer, S.-W. Li, S. Zhang, R. James, G. Ghosh, Y. Taigman, M. Fazel-Zarandi, A. Celikyilmaz, L. Zettlemoyer, A. Aghajanyan, Scaling autoregressive multi-modal models: Pretraining and instruction tuning (2023). [arXiv:2309.02591](https://arxiv.org/abs/2309.02591). URL <https://arxiv.org/abs/2309.02591>
- [7] D. Podell, Z. English, K. Lacey, A. Blattmann, T. Dockhorn, J. Müller, J. Penna, R. Rombach, Sdxl: Improving latent diffusion models for high-resolution image synthesis (2023). [arXiv:2307.01952](https://arxiv.org/abs/2307.01952). URL <https://arxiv.org/abs/2307.01952>
- [8] L. Zhang, A. Rao, M. Agrawala, Adding conditional control to text-to-image diffusion models (2023). [arXiv:2302.05543](https://arxiv.org/abs/2302.05543). URL <https://arxiv.org/abs/2302.05543>
- [9] H. Ye, J. Zhang, S. Liu, X. Han, W. Yang, Ip-adapter: Text compatible image prompt adapter for text-to-image diffusion models (2023). [arXiv:2308.06721](https://arxiv.org/abs/2308.06721). URL <https://arxiv.org/abs/2308.06721>
- [10] E. J. Hu, Y. Shen, P. Wallis, Z. Allen-Zhu, Y. Li, S. Wang, L. Wang, W. Chen, Lora: Low-rank adaptation of large language models (2021). [arXiv:2106.09685](https://arxiv.org/abs/2106.09685). URL <https://arxiv.org/abs/2106.09685>
- [11] T. Dettmers, A. Pagnoni, A. Holtzman, L. Zettlemoyer, Qlora: Efficient finetuning of quantized llms (2023). [arXiv:2305.14314](https://arxiv.org/abs/2305.14314). URL <https://arxiv.org/abs/2305.14314>
- [12] Q. Wang, Y. Fan, J. Bao, H. Jiang, Y. Song, Bora: Bi-dimensional weight-decomposed low-rank adaptation (2024). [arXiv:2412.06441](https://arxiv.org/abs/2412.06441). URL <https://arxiv.org/abs/2412.06441>
- [13] K. Zhou, J. Yang, C. C. Loy, Z. Liu, Learning to prompt for vision-language models, *International Journal of Computer Vision* 130 (9) (2022) 2337–2348. doi:10.1007/s11263-022-01653-1. URL <http://dx.doi.org/10.1007/s11263-022-01653-1>
- [14] M. Jia, L. Tang, B.-C. Chen, C. Cardie, S. Belongie, B. Hariharan, S.-N. Lim, Visual prompt tuning (2022). [arXiv:2203.12119](https://arxiv.org/abs/2203.12119). URL <https://arxiv.org/abs/2203.12119>
- [15] N. Ruiz, Y. Li, V. Jampani, Y. Pritch, M. Rubinstein, K. Aberman, Dream-booth: Fine tuning text-to-image diffusion models for subject-driven generation (2023). [arXiv:2208.12242](https://arxiv.org/abs/2208.12242). URL <https://arxiv.org/abs/2208.12242>
- [16] K. Agrawal, R. Banerjee, Synthetic art generation and deepfake detection: A study on jamini roy inspired dataset, *TechRxiv* (Mar. 2025). doi:10.36227/techrxiv.174119231.19482547/v1. URL <http://dx.doi.org/10.36227/techrxiv.174119231.19482547/v1>
- [17] R. Gal, Y. Alaluf, Y. Atzmon, O. Patashnik, A. H. Bermanto, G. Chechik, D. Cohen-Or, An image is worth one word: Personalizing text-to-image generation using textual inversion (2022). [arXiv:2208.01618](https://arxiv.org/abs/2208.01618). URL <https://arxiv.org/abs/2208.01618>
- [18] W. Dai, L. Lu, Z. Li, Diffusion-based synthetic data generation for visible-infrared person re-identification (2025). [arXiv:2503.12472](https://arxiv.org/abs/2503.12472). URL <https://arxiv.org/abs/2503.12472>
- [19] Z. Zhang, T. Zhao, Y. Guo, J. Yin, Rs5m and georsclip: A large-scale vision-language dataset and a large vision-language model for remote sensing, *IEEE Transactions on Geoscience and Remote Sensing* 62 (2024) 1–23. doi:10.1109/tgrs.2024.3449154. URL <http://dx.doi.org/10.1109/TGRS.2024.3449154>
- [20] S. Khanna, P. Liu, L. Zhou, C. Meng, R. Rombach, M. Burke, D. Lobell, S. Ermon, Diffusionsat: A generative foundation model for satellite imagery (2024). [arXiv:2312.03606](https://arxiv.org/abs/2312.03606). URL <https://arxiv.org/abs/2312.03606>
- [21] Z. Yu, C. Liu, L. Liu, Z. Shi, Z. Zou, Metaearth: A generative foundation model for global-scale remote sensing image generation (2024). [arXiv:2405.13570](https://arxiv.org/abs/2405.13570). URL <https://arxiv.org/abs/2405.13570>
- [22] D. Tang, X. Cao, X. Hou, Z. Jiang, J. Liu, D. Meng, Crs-diff: Controllable remote sensing image generation with diffusion model (2024). [arXiv:2403.11614](https://arxiv.org/abs/2403.11614). URL <https://arxiv.org/abs/2403.11614>
- [23] L. Pang, X. Cao, D. Tang, S. Xu, X. Bai, F. Zhou, D. Meng, Hsigene: A foundation model for hyperspectral image generation (2024). [arXiv:2409.12470](https://arxiv.org/abs/2409.12470). URL <https://arxiv.org/abs/2409.12470>
- [24] C. Liu, K. Chen, R. Zhao, Z. Zou, Z. Shi, Text2earth: Unlocking text-driven remote sensing image generation with a global-scale dataset and a foundation model (2025). [arXiv:2501.00895](https://arxiv.org/abs/2501.00895). URL <https://arxiv.org/abs/2501.00895>
- [25] Z. Ma, X. Xiao, S. Dong, P. Wang, H. Wang, Q. Pan, Sarchat-bench-2m: A multi-task vision-language benchmark for sar image interpretation (2025). [arXiv:2502.08168](https://arxiv.org/abs/2502.08168). URL <https://arxiv.org/abs/2502.08168>
- [26] W. Hong, W. Wang, M. Ding, W. Yu, Q. Lv, Y. Wang, Y. Cheng, S. Huang, J. Ji, Z. Xue, L. Zhao, Z. Yang, X. Gu, X. Zhang, G. Feng, D. Yin, Z. Wang, J. Qi, X. Song, P. Zhang, D. Liu, B. Xu, J. Li, Y. Dong, J. Tang, Cogvlm2: Visual language models for image and video understanding (2024). [arXiv:2408.16500](https://arxiv.org/abs/2408.16500). URL <https://arxiv.org/abs/2408.16500>
- [27] R. M. Haralick, K. Shanmugam, I. Dinstein, Textural features for image

- classification, *IEEE Transactions on Systems, Man, and Cybernetics SMC-* 3 (6) (1973) 610–621. doi:10.1109/TSMC.1973.4309314.
- [28] A. Kirillov, E. Mintun, N. Ravi, H. Mao, C. Rolland, L. Gustafson, T. Xiao, S. Whitehead, A. C. Berg, W.-Y. Lo, P. Dollár, R. Girshick, Segment anything (2023). *arXiv:2304.02643*.
URL <https://arxiv.org/abs/2304.02643>
- [29] S. Debuysère, N. Trouvé, N. Letheule, E. Colin, O. Lévêque, Synthesizing sar images with generative ai: Expanding to large-scale imagery, <https://hal.science/hal-04786104> (October 2024).
- [30] S. Debuysère, N. Trouvé, N. Letheule, O. Lévêque, E. Colin, From space-born to airborne: Sar image synthesis using foundation models for multi-scale adaptation (2025). *arXiv:2505.03844*.
URL <https://arxiv.org/abs/2505.03844>